ingegneria sismica
International Journal of Earthquake Engineering
Anno XLIII - Num. 1 - 2026

# Research on the information loading strategy of electric power IOT devices based on wireless positioning data transmission

*Hui Zhang*[1], *Xiaofeng Lu*[1,*], *Kai Kang*[1], *Huabo Mao*[1], *Honghong Zhu*[1] *and Dawei Shao*[1]

[1] Jinhua Power Transmission and Transformation Engineering Co., Ltd. Sanwei Electric Power Branch, Jinhua, Zhejiang, 310000 China

**SUMMARY:** *In the context of the internet of things, dynamic loading of device data information has gained greater importance over time. The proposed algorithm is a Geometric Constraint-based Least Squares Estimation (GC-LSE) positioning algorithm. Accuracy of positioning data is improved by enforcing distance boundary constraints and equality constraints between device reference points and unknown nodes. This strategy makes it possible to monitor operation data of surge arresters and transformers online. Variable fractional delay (VFD) filter is developed on the basis of Farrow structure. Data are processed in two stages, i.e., integer point delay then fraction multiple delay to allow dynamic information loading of IoT devices. Once the positioning errors have been corrected and filtered delays have been processed, the mean information loading time to power IoT devices is only 2.30 seconds with a success rate of 99.19-100.00 percentage, which proves that the optimized loading strategy is effective.*

***KEYWORDS:*** *Geometric Constraint; GC-LSE; VFD Filter; Delay Processing; Power IoT Device*

## 1 Introduction

The intelligent grids have self-healing, interactivity, optimization, compatibility and integration that facilitate information exchange and interaction between the equipment of the grid systems [1-2]. The implementation of the IoT technology under the smart grid paradigm broadens the idea beyond the system intelligence to the intelligence of the power IoT devices [3, 4].. Information of power IoT devices is multi-source and very heterogeneous, requiring the solution to the problem of multi-source data heterogeneity in the process of the aggregation [5]. By using the latest communication, networking, positioning as well as software technologies, real-time loading and localisation of power IoT device information into smart grid zones is effectively able to remove safety threats in production processes and maintenance [6-8]. Wireless sensor networks provide the smart grid operation safety management system with accurate positioning and showing the real-time location data on substation floor plans. Various work groups are denoted by other colored markers in order to be visually distinguishable [9, 10].

The power system has a large scale, is composed of a large number of IoT devices, and has an intricate inner structure. It produces huge volumes of power data in the generation, transmission, transformation, distribution, dispatch and consumption processes. Such data is important in management of the power system and business operations [11-13]. Development

*zhydc169@163.com
https://doi.org/10.65102/is2026474
Published: 30 April, 2026

of smart sensor technology is also fast offering more options to monitor power IoT devices online [14]. Intelligent sensors have the ability to monitor at high frequency with high precision and can be used to measure multidimensional parameters including temperature, vibration, current, and voltage of an IoT device in real time. The information is delivered over wireless communication technologies to cloud platforms where it is processed and analyzed centrally [15-17].

The direction of change in the Chinese power industry is now gradually moving towards knowledge-based and technologically oriented operations. Loading of relevant data information is part of an important duty in this industry [18, 19]. The transmission models of data changes as the size of power systems does so as well, and all of them have different features. Therefore, it is necessary to choose the right mode of data transmission of power IoT equipment to ensure that the power industry really progresses and satisfies the modern needs of society [20, 21]. Implementation of wireless positioning data transmission technologies in loading information of power IoT devices replacing manual control with technical solutions is of revolutionary value in the safe functioning of smart grids.

The paper combines wireless positioning with data transmission to improve the real-time reliability of data loading of power IoT devices and minimize energy usage. Positioning errors can be greatly reduced by using geometric limits of node distances, which are used as boundary conditions on device locations, and by changing distance correction coefficients. A more effective resistive fundamental current method is chosen in order to monitor and extract operational data in surge arresters and transformers. Dynamic information loading is obtained by either power or delay variation analysis. The importance of delay information being recognized, VFD filters are used to calculate parameters and segment data sampling intervals. This allows loading of dynamic delay information precisely by sequentially applying integer-multiple sampling interval delays and fractional-multiple sampling interval delays.

# 2 Loading of Power IoT Device Information Based on Wireless Positioning Optimization

## 2.1 Geometry-Based Constraint Optimization for Wireless Positioning

To effectively load information on power IoT devices, it is necessary to transmit wireless positioning data with some accuracy. The section suggests a geometry-constraint based wireless positioning optimization scheme, which improves positioning accuracy by measuring the distance and adjusting the correction coefficient.

This optimization scheme, termed the Geometric Constraint-based Least Squares Estimation (GC-LSE) positioning algorithm, primarily refines the least squares estimation method. It leverages the geometric constraints between distances from four reference points to an unknown node, correcting the four measured distances to eliminate the impact of unreasonable ranging errors on positioning results, thereby enhancing positioning accuracy.

Regarding the deployment method of reference points, the positioning effect achieved by arranging them in regular geometric shapes is optimal. Therefore, this paper selects regular rectangles as the arrangement method for reference points. For illustrative convenience, the coordinates of reference nodes are simplified. It is assumed that the reference points form a rectangle with length $m$ and width $n$, and a coordinate system is established with the lower-left corner point as the origin. The coordinates of the four reference points are thus $(0,0),(m,0),(0,n),(m,n)$, where $x_1=0, y_1=0, x_2=0, y_2=0, x_3=0, y_3=0, x_4=0, y_4=n$. Therefore:

$$\begin{cases} x^2 + y^2 = d_1^2 \\ (x-m)^2 + y^2 = d_2^2 \\ x^2 + (y-n)^2 = d_3^2 \\ (x-m)^2 + (y-n)^2 = d_4^2 \end{cases} \tag{1}$$

$$\begin{cases} 2mx = d_1^2 - d_2^2 \\ 2my = d_1^2 - d_3^2 \\ 2mx + 2my = d_1^2 - d_4^2 \end{cases} \tag{2}$$

$$A = \begin{bmatrix} m & 0 \\ 0 & n \\ m & n \end{bmatrix}, b = \begin{bmatrix} b_1 \\ b_2 \\ b_3 \end{bmatrix} = \begin{bmatrix} d_1^2 - d_2^2 \\ d_1^2 - d_3^2 \\ d_1^2 - d_4^2 \end{bmatrix} \tag{3}$$

$$\begin{aligned} X &= \frac{1}{2}\left(A^T A\right)^{-1} A^T b = \frac{1}{2}\begin{bmatrix} \frac{2}{3m} & -\frac{1}{3m} & \frac{1}{3m} \\ -\frac{1}{3n} & \frac{2}{3n} & \frac{1}{3n} \end{bmatrix}\begin{bmatrix} b_1 \\ b_2 \\ b_3 \end{bmatrix} \\ &= \begin{bmatrix} \frac{1}{6m}\left(2b_1 - b_2 + b_3\right) & \frac{1}{6n}\left(-b_1 + 2b_2 + b_3\right) \end{bmatrix} \end{aligned} \tag{4}$$

Subtracting equation 1 from equation 3 and equation 2 from equation 4 in system (1) yields the geometric constraints between the pairs $d_1, d_2, d_3, d_4$ (1).

### 2.1.1 Distance Boundary Constraints

Based on geometric relationships, within the rectangular positioning area, the distance between two points is constrained by the rectangle's length and width. If we define the differences between the two distances as $\alpha = d_3^2 - d_1^2 = n^2 - 2yn, \beta = d_4^2 - d_2^2 = n^2 - 2yn$, then

$$\begin{aligned} -n^2 \le \alpha \le n^2 \\ -n^2 \le \beta \le n^2 \end{aligned} \tag{5}$$

Due to environmental interference in actual testing scenarios, abnormal situations frequently occur where measured RSSI values exceed the theoretical mean. After conversion to distance, the measured distance is approximately 2.0 times greater than the actual distance. This causes significant bias in the positioning results, yielding completely unreasonable locations. At this point, if $d_1, d_2, d_3, d_4$ are substituted into equation (5) for verification, it is found that the inequality in the equation is no longer satisfied. Therefore, for the above anomaly, the following handling can be applied:

When $\alpha \gg n^2$, it indicates that $d_3$ is abnormal. Reduce $\alpha$ to the boundary value $n^2$ to correct $d_3$ as much as possible within a reasonable range. The specific correction method is:

$$d_3^2 = d_1^2 + n^2 \tag{6}$$

Then, the revised positioning calculation result becomes

$$\hat{X}^T = \begin{bmatrix} \frac{1}{6m}\left(2b_1 - \left(b_2 + \alpha - n^2\right) + b_3\right) \\ \frac{1}{6n}\left(-b_1 + 2\left(b_2 + \alpha - n^2\right) + b_3\right) \end{bmatrix} \tag{7}$$

The difference between the corrected calculation result and the original calculation result is the correction distance.

$$X_e = X - \hat{X} = \begin{bmatrix} \frac{1}{6m}\left(\alpha - n^2\right) \frac{1}{6n}\left(\alpha - n^2\right) \end{bmatrix} \tag{8}$$

As shown above, boundary-constrained correction can significantly reduce the positioning error of $X_e$, and the optimization effect on $X_e$ increases with increasing $\alpha$. Generally, when the ranging error causes $\alpha \gg n^2$, the optimization improvement from the above correction method becomes more pronounced. It corrects originally unreasonable calculation results to a reasonable range, bringing the estimated position closer to the actual unknown node location.

Similarly, when $\alpha \ll n^2$, it indicates an anomaly in $d_1$. The correction method is:

$$d_1^2 = d_3^2 + n^2 \tag{9}$$

When the measured value of $d_4$ is an outlier, $\beta \gg n^2$. The corresponding correction method in this case is

$$d_4^2 = d_2^2 + n^2 \tag{10}$$

When the measured value of $d_2$ is an outlier, $\beta \ll -n^2$. The corresponding correction method is

$$d_2^2 = d_4^2 + n^2 \tag{11}$$

### 2.1.2 Distance Equality Constraint

The distance-based equality constraint leverages the geometric relationship among four distances to reduce the probability of errors by $d_1, d_2, d_3, d_4$ and enhance the accuracy of positioning results. The specific equality constraints are as follows:

$$d_1^2 + d_4^2 = d_2^2 + d_3^2 = x^2 + y^2 + (x-m)^2 + (y-n)^2 \tag{12}$$

When equation (12) does not hold, it indicates the presence of errors in the test distances $d_1, d_2, d_3, d_4$. These errors primarily stem from unavoidable objective factors such as operational inaccuracies or variations in hardware equipment. Furthermore, extensive testing has demonstrated that the received signal strength indicator (RSSI) tends to be low during the testing process, meaning the measured distances are inflated. Let $\Delta = \left(d_1^2 + d_4^2\right) - \left(d_2^2 + d_3^2\right)$. When $\Delta > 0$, $d_1$ and $d_4$ are relatively large. Since measured RSSI values are often

underestimated, this leads to an overestimated test distance. Therefore, $d_1$ and $d_4$ require correction at this point. Considering that the likelihood of error increases with distance, the present invention reasonably adjusts the correction coefficients for both. The specific correction method is as follows:

$$\begin{aligned} d_1^2 &= d_1^2 - \frac{d_1^2}{d_1^2 + d_4^2}\Delta \\ d_4^2 &= d_4^2 - \frac{d_4^2}{d_1^2 + d_4^2}\Delta \end{aligned} \tag{13}$$

Similarly, when $\Delta < 0$, $d_2$ and $d_3$ require correction as follows:

$$\begin{aligned} d_2^2 &= d_2^2 - \frac{d_2^2}{d_2^2 + d_3^2}\Delta \\ d_3^2 &= d_3^2 - \frac{d_3^2}{d_2^2 + d_3^2}\Delta \end{aligned} \tag{14}$$

Optimization schemes based on boundary constraints are primarily applicable when two or one test distance exhibits significant error. Optimization schemes based on equality constraints are primarily applicable when only one of the four test distances exhibits significant error. These two optimization schemes are not mutually exclusive and can be used concurrently. When both schemes are employed simultaneously, the improvement in positioning accuracy is more pronounced. Therefore, it is generally advisable to adopt both approaches concurrently. The optimization schemes are applied in simulation experiments in this paper, which shows their effectiveness and legitimacy.

## 2.2 Online Monitoring Solution for Power IoT Devices

### 2.2.1 Online Monitoring Technology Solution for Surge Arresters

After a long period of work, surge arresters can have a chain of possible hazards caused by environmental conditions and voltage changes. Some typical hazards are aged valve discs, water penetration in insulation, and thermal failure. To monitor surge arresters online, one can use the total current method, third harmonic method, or capacitive current compensation method. Though several technical options can be used, each has its own benefits and drawbacks in practice. Full-current method is unable to indicate aging problems with surge arresters, the third-harmonic method can easily be interfered by system harmonics, and the capacitive current compensation method does not have enough stability. Because of these factors, the research process has adopted a refined resistive fundamental current method to keep track of the working condition of surge arresters. This strategy is effective to eliminate the disadvantages of other strategies especially when it comes to eliminating harmonic interference.

When the voltage contains only fundamental components, let the fundamental voltage component be denoted as $u$, then:

$$u = U_m \sin(\omega t) \tag{15}$$

In the equation: $U_{\mathrm{m}}$ represents the maximum voltage amplitude; $\omega$ denotes the voltage

frequency; $t$ signifies time. The resistance of zinc oxide surge arresters exhibits nonlinear characteristics. Under these conditions, high-order harmonic components $i_{\mathrm{R}}$ will be generated in the resistive current of the arrester. This component can be expressed as in formula (16):

$$i_R = i_1 + i_2 + \cdots + i_n = I_{1m}\sin\left(\omega t + \varphi_n\right) + \cdots + I_{nm}\sin\left(n\omega t + \varphi_n\right) \tag{16}$$

In the equation: $i_1, i_2, \cdots, i_n$ represent different high-frequency harmonic components; $i_R$ is the sum of harmonic components at all frequencies; $I_{km}$ is the $i$ th harmonic current, where $k = 1, 2, \cdots, n$; $\varphi_n$ is the phase angle of the current. The valve discs of zinc oxide surge arresters incur a certain power loss W during operation, calculated using formula (17):

$$W = \int_0^t \sum_{i=1}^{n} I_{km}\sin\left(k\omega t + \varphi_n\right) \times u dt \tag{17}$$

According to Formula (17), the power consumption of zinc oxide surge arresters primarily originates from the fundamental component of resistive current, while higher harmonic components do not cause power loss.

The resistive fundamental current extraction process is as follows: A small current transformer collects the operating current of the arrester → A low-pass filter obtains the fundamental current → A waveform conversion circuit acquires the phase angle difference → The resistive fundamental current is derived from the fundamental current and phase angle difference. Within the master station system, resistive fundamental current extraction involves three stages: total leakage current collection, extraction of the fundamental component from the total leakage current, and extraction of the resistive fundamental current.

### 2.2.2 Online Monitoring Technology Solution for Transformers

Taking the S-series oil-immersed transformer as the analysis subject, monitored indicators include winding temperature, oil level, partial discharge, abnormal noise, load, and the structural temperature of the transformer's top layer. The following introduces online monitoring methods for some of these indicators.

Abnormal increases in oil temperature often indicate potential safety hazards in the transformer's insulation, making it a key focus for online monitoring. Sensors for oil temperature monitoring can be either PT100 or DS18B20. The former converts resistance values into corresponding oil temperatures, while the latter is a direct-reading temperature sensor. Taking the PT100 metal foil probe as an example, its resistance-to-temperature conversion relationship is given by Formula (18):

$$\begin{cases} R_t = 100\left[1 + At' + Bt'^2 + C\left(t' - 100\right)t'^3\right], -200 \le t' \le 0 \\ R_t = 100\left(1 + At' + Bt'^2\right), 0 \le t' \le 850 \end{cases} \tag{18}$$

In the equation: $R_{t'}$ represents the resistance value of the metal probe; $t'$ denotes the oil temperature; $A, B, C$ are three distinct constants. The study employs PT100 temperature sensors. The oil temperature sampling process is as follows: resistance sampling → voltage sampling → upload to RTU → obtain oil temperature data through calculation or table lookup → upload to the master station system server → temperature query and display.

Transformers comprise numerous components. During normal operation, their sound

remains stable. However, upon fault occurrence, abnormal noises may arise, often caused by vibrations of the transformer casing or expansion/contraction of internal silicon steel laminations. Monitoring these noises employs acoustic sensors, utilizing MIC microphones as sound source acquisition components. The sensors implement audio amplification circuits based on the LM386 chip. The sensor outputs a voltage signal ranging from 0 to 5V. When transformer noise exceeds Level 2 warning thresholds, field inspection is required to identify the root cause.

## 2.3 Power IoT Device Information Loading Method

### 2.3.1 Principles and Implementation of Dynamic Information Loading

Under ideal conditions, the relationship between the received signal $S_\tau(t)$ and the transmitted signal $S_s(t)$ can be expressed as

$$S_\tau(t) = kS_s(t-\tau) \tag{19}$$

In the equation: $\tau$ represents the signal transmission delay; $k$ denotes the signal amplitude attenuation.

As shown in Equation (19), the dynamic information loaded during dynamic signal simulation includes power (i.e., amplitude) variation information and delay variation information. Power variation information is primarily related to the propagation distance of electromagnetic waves and channel characteristics. In practical simulations, this can be achieved using power attenuators, whose implementation is relatively straightforward. Therefore, this paper focuses on the loading of delay information.

Since filters exhibit group delay effects on transmitted signals, and this group delay is linearly controllable within the passband, delay information loading can be achieved by precisely controlling the group delay of digital filters. However, conventional finite-impulse response (FIR) filters have fixed group delays, and the delay is an integer multiple of the sampling interval. Such filters exhibit low precision in dynamic simulation and require frequent parameter adjustments based on delay information, demanding high system real-time performance.

To address the issue of continuously variable fractional group delay in conventional filters, a variable fractional delay (VFD) filter based on the Farrow structure is proposed. The frequency response of the Farrow structure filter depends on the fractional delay, but the filter coefficients are independent of the delay. Therefore, in practical applications, the filter coefficients need to be computed and stored only once. A limitation of the VFD filter for signal delay processing is that the original data must first undergo integer-point delay processing.

Based on the characteristics of the VFD filter, Figure 1 illustrates a proposed delay filter implementation for dynamic information loading.

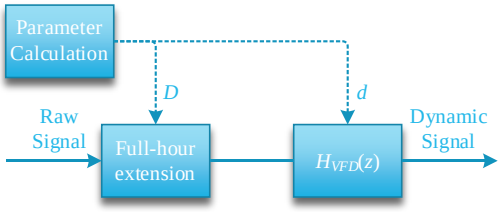


*Figure 1: Dynamic loading scheme based on VFD filter*

The parameter calculation module computes the precise delay corresponding to the raw data based on orbital parameters, dividing this delay into integer multiples of the sampling interval delay $D$ and fractional multiples of the sampling interval delay $d(0 \leqslant d < 1)2$. The integer delay module first applies the integer delay $D$ to the original data based on the parameter, then incorporates fractional delays through the VFD filter, thereby loading dynamic delay information onto the original data.

### 2.3.2 Design and Simulation of Delay Filters

Assume $x(t)$ is a continuous-time signal. After applying a $\tau$ delay to $x(t)$, its delayed signal is obtained as

$$y(t) = x(t - \tau) \tag{20}$$

Sampling $x(t), y(t)$ yields the discrete signals $x(n)$ and $y(n)$, respectively.

$$y(n) = x\left(n - D_\tau\right) \tag{21}$$

In the formula: $D_\tau = \tau / T_s$, $T_s$ is the sampling period. Typically, the delay value $\tau$ is not an integer multiple of the sampling interval. Therefore, the digital delay value $D_\tau$ can be expressed as $D_\tau \lfloor D \rfloor + d$, where $\lfloor D \rfloor$ denotes the largest integer less than $D_\tau$, and $d$ represents the fractional part of $D_\tau$.

Applying the Discrete-Time Fourier Transform (DTFT) to the delayed output signal $y(n)$ yields:

$$Y(\omega) = \sum_{n=-\infty}^{\infty} y(n) e^{-j\omega m} = \sum_{n=-\infty}^{\infty} x\left(n - D_\tau\right) e^{-j\omega m} = X(\omega) e^{-j\omega D_\tau} \tag{22}$$

In the equation: $Y(\omega), X(\omega)$ denote the discrete-time Fourier transforms of $y(n)$ and $x(n)$, respectively.

From equation (22), the response function of the delayed system can be expressed as

$$H_{id}(\omega) = \frac{Y(\omega)}{X(\omega)} = e^{-j\omega D_\tau}, |\omega| \leqslant \pi \tag{23}$$

Since the ideal filter is physically unrealizable, it is generally realized by approximating $h_{id}(n)$ with $N$-order finite-length FIR filters $h(n)$, and the system corresponds to a frequency response of

$$H\left(e^{j\omega}\right) = \sum_{n=0}^{N} h(n) e^{-j\omega n} \tag{24}$$

If the filter coefficients $h(n)$ are approximated by a polynomial of order $M$ with fractional delay $d$, the parameter $d$ can be separated from the filter coefficients, and here, taking into account the convergence of the polynomials, only the fractional part of the delay $D_\tau$ is taken into account, and $h(n)$ in equation (24) can be defined as

$$h(n,d)=\sum_{m=0}^{M} c(n,m)d^m, 0\leqslant d<1 \tag{25}$$

Substituting equation (25) into (24) yields

$$H(z,d)=\sum_{n=0}^{N}\left[\sum_{m=0}^{M-1} c(n,m)d^m\right]z^{-n}=\sum_{m=0}^{M-1}\left[\sum_{n=0}^{N} c(n,m)z^{-n}\right]d^m=\sum_{m=0}^{M-1} C_m(n)d^m \tag{26}$$

From equation (26), it can be seen that $H(z,d)$ can be regarded as the weighted sum of the outputs of $M$ $N$ th-order direct-form FIR filters $C_m(n)$ with a fractional delay $d$. Although the filter's frequency response depends on the fractional delay $d$, the coefficients of each branch filter are independent of the delay value $d$. Therefore, recalculating or reloading the filter coefficients is unnecessary when the delay value $d$ changes.

This paper designs a VFD filter based on the proposed weighted least squares (WLS) algorithm-based VFD filter design method. The WLS algorithm defines the frequency response weighted error function as

$$J=\int_0^{\pi}\int_0^{1} W(\omega,p)\left|H(\omega,p)-H_{id}(\omega,p)\right|^2 d\omega dp \tag{27}$$

$$W(\omega,p)=W_1(\omega)W_2(p) \tag{28}$$

In the formula: $W_1(\omega)$ and $W_2(p)$ are respectively

$$W_1(\omega)=\begin{cases}0.640, & \omega\in[0,0.550\pi)\\ 4.900, & \omega\in[0.550\pi,0.850\pi)\\ 37.000, & \omega\in[0.850\pi,0.899\pi)\\ 0.000, & \omega\in[0.899\pi,\pi)\end{cases} \tag{29}$$

$$W_2(p)=\begin{cases}53.000, & p\in[0.000,0.100)\\ 0.200, & p\in[0.100,0.900)\\ 8.000 & p\in[0.900,1.000)\end{cases} \tag{30}$$

For convenience of expression, introduce independent variable $p(p=d)$. Define the absolute error expression as

$$e(\omega,p)=20\lg\left|H(\omega,p)-H_{id}(\omega,p)\right| \tag{31}$$

# 3 Information Loading Practices Under the Optimized Solution

## 3.1 Wireless Positioning Optimization Solution Verification

### 3.1.1 Test and Validation Scenario Analysis

This instance selects the commercial district of City A at 10:00 AM on June 19, 2025, as the testing and validation scenario for the wireless positioning optimization solution. Figure 2 depicts the test area within an urban environment, where solid thick lines indicate the test area boundaries and dashed lines represent measurement paths along the predicted area boundaries. Data collected along this path will be used to measure the distance boundaries of various power IoT devices within the test area, thereby obtaining preliminary positional information between these devices. Paths marked with "-" within the prediction area represent test paths for verifying data. The given data is utilized to assess results of measurements and confirm results of positioning. Character A, B, C, and D stands to indicate the four base stations that house various power IoT devices. Five-pointed stars are used to mark the base station locations next to the characters. The size of this area, measured in a straight line, is about 800 meters both in length and breadth. The real perimeter path has an irregular form. The power IoT devices base stations are spread out almost even, which satisfies the test conditions of the wireless positioning distance constraint plan.

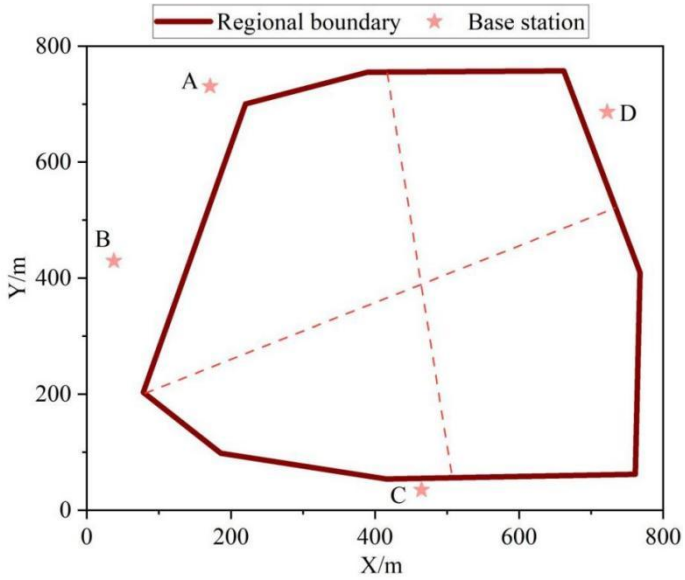


*Figure 2: Testing and verification scenarios*

### 3.1.2 Evaluation of Positioning Results

A least-squares estimation positioning algorithm based on geometric constraints locates specific power IoT devices within the prediction area. By applying boundary constraints and equality constraints, it corrects the positions of reference points for power IoT devices and estimates the node locations of unknown power IoT devices. Since the correction coefficient affects the final positioning error, positioning errors under different correction coefficients α are compared to determine the optimal correction coefficient.

Figure 3 shows the positioning results for unknown nodes when α=0.65. Figure 4 displays the statistical percentage and cumulative percentage of absolute positioning errors. With α=0.65,

the actual position of the unknown node's power IoT device is (x,y)=(430.47445,682.35294)m. 66.67% of the measured points exhibited positioning errors ranging from 16.24 to 91.24 meters, while the remaining 33.33% had errors between 109.31 and 167.88 meters. The error percentage range was [0.004, 0.390]%.

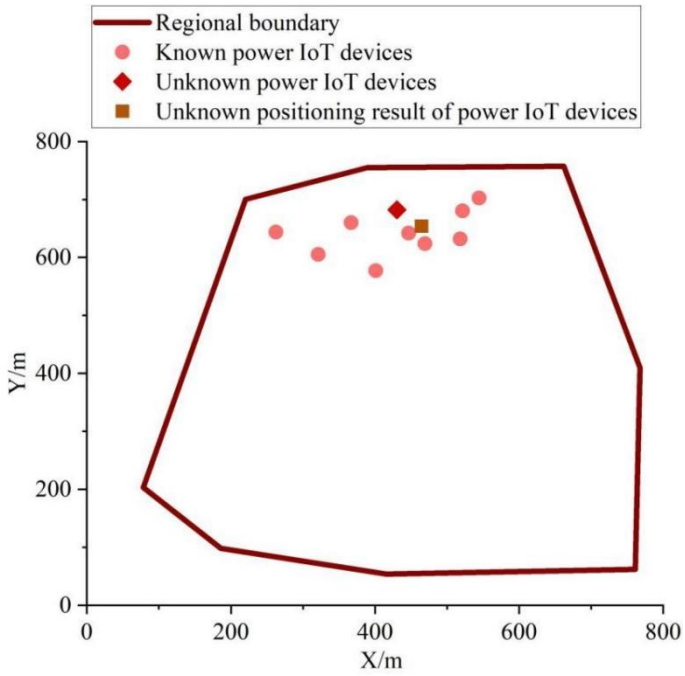


*Figure 3: α=0.65,The positioning result of the unknown node*

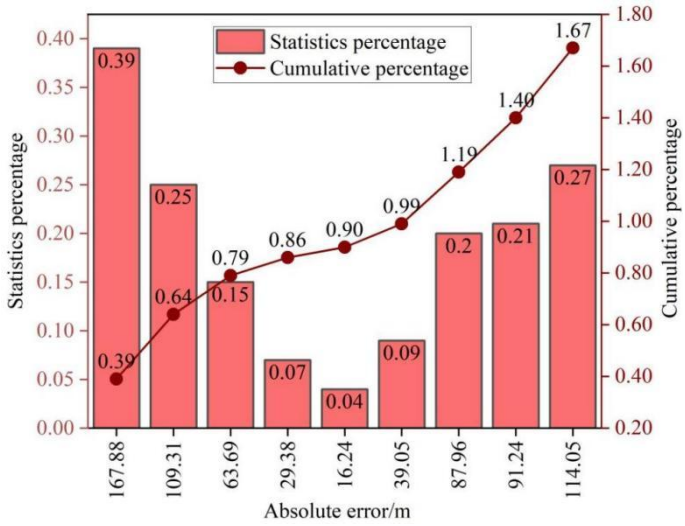


*Figure 4: α=0.65,statistics and cumulative % of absolute positioning errors*

Figure 5 shows the positioning results for unknown nodes when the correction coefficient α = 0.45. Figure 6 displays the statistical percentage and cumulative percentage of absolute positioning errors. With a correction coefficient α=0.45, 66.67% of the measured points had positioning errors ranging from 6.57 to 88.14 meters, while the remaining 33.33% had errors between 131.93 and 172.81 meters. The error percentage range was [0.002, 0.40]%.

When the correction coefficient α = 0.45, the algorithm's positioning error is relatively larger than when α = 0.65. This aligns with the constraint that a larger α yields better correction

effects. Therefore, selecting α = 0.65 as the algorithm parameter reduces the positioning error level of power IoT devices.

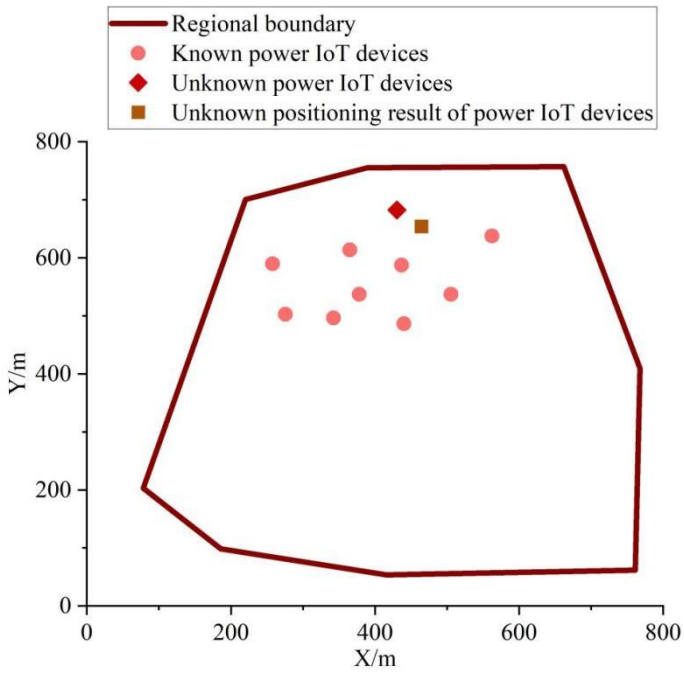


*Figure 5: α=0.45,The positioning result of the unknown node*

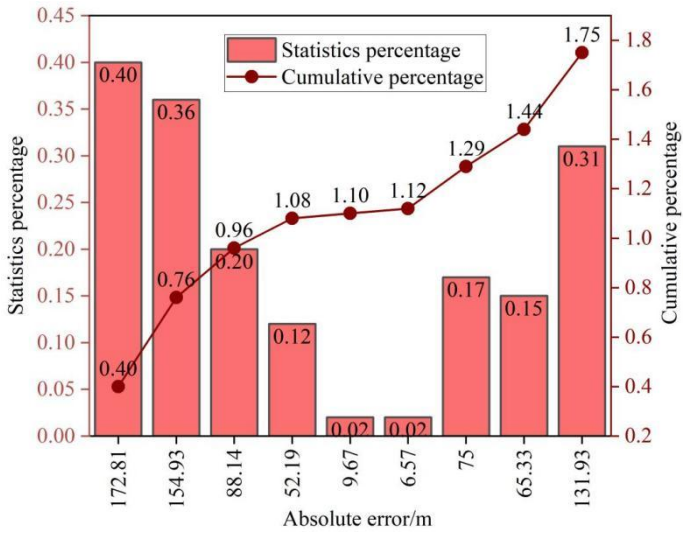


*Figure 6: α=0.45,statistics and cumulative % of absolute positioning errors*

## 3.2 Data Processing During Dynamic Information Loading

### 3.2.1 Overall Power Attenuation of Data

Online monitoring of a specific surge arrester within the target area is performed by collecting its electromagnetic wave signals using an improved resistive fundamental current method. Due to limitations such as the arrester's inherent aging, overall power attenuation processing is applied to the signal data prior to dynamic information loading delay processing. This reduces errors in dynamic information loading caused by physical equipment damage or other factors. Figure 7 compares the electromagnetic spectrum before and after overall power attenuation and

segmented processing using a power attenuator. Prior to overall attenuation, the normalized frequency range of the collected signal spans 0.0–1.0, with the overall power range between 0W and 180W. After attenuation with the power attenuator, the normalized frequency concentrated between 0.30 and 1.00, with the overall power range narrowing to 0W–120W. Following overall power attenuation, the signal range fluctuations of this power IoT device became smaller and more aligned with actual conditions. Simultaneously, the electromagnetic wave information content could be calculated more clearly, facilitating subsequent delay processing.

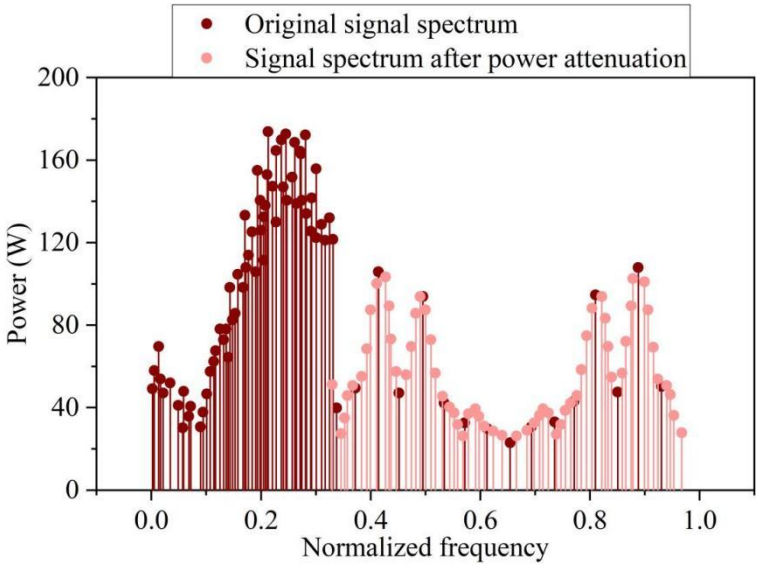


*Figure 7: Power attenuation and signals before and after segmented processing*

### 3.2.2 Delay Filter Processing

Apply time delay processing to the original data after overall power attenuation. First, use the integer-point delay module to apply integer-point delay to the original data. Then, introduce fractional delay through the VFD filter, thereby loading dynamic delay information onto the original data. Figure 8 shows the time-domain effect of the data after integer-point delay. Figure 9 shows the time-domain effect of the data after introducing fractional delay. After undergoing both integer-point delay and VFD filter fractional delay, the information amplitude remains within its original range. However, the data distribution shifts from its original concentration between 0.0s and 1.0s to a delayed range spanning 1.0s to 2.0s, ultimately clustering between 0.8s and 1.6s. This approach prevents information congestion during dynamic loading that could cause data loss while ensuring real-time loading performance.

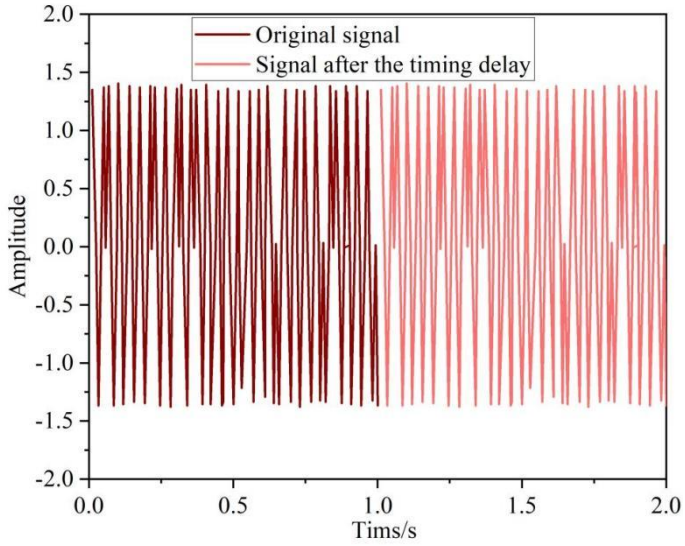


*Figure 8: Time-domain effect of the data after the timing adjustment*

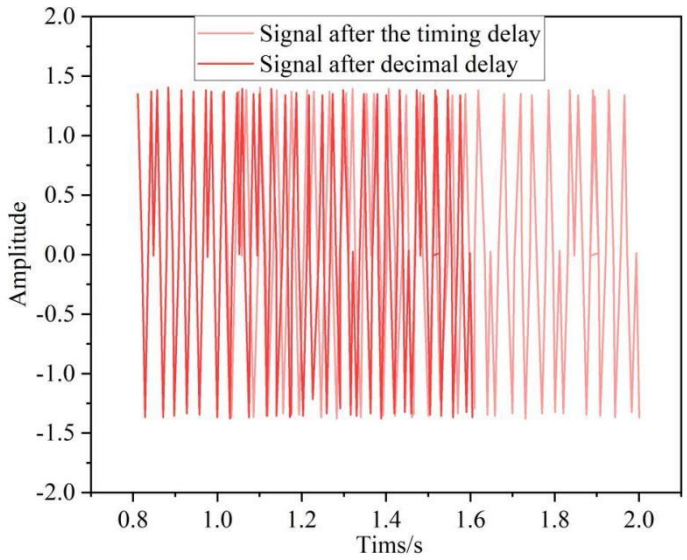


*Figure 9: Time-domain effect of the data after adding decimal delay*

## 3.3 Real-Time Information Loading Practice Based on Wireless Positioning Data

To validate the effectiveness of the improved information loading method for power IoT devices described in this paper and test its real-time dynamic loading functionality, loading experiments were conducted on hardware boards. A dynamic loading module was embedded within the FPGA program on the software compilation platform, enabling the loading of preprocessed arrester raw data in mcs file format onto the platform. For this validation of real-time dynamic information loading, five mcs files totaling 60.0MB in size were selected. After powering down the FPGA board, the FPGA continuously simulated dynamic loading trigger signals sent by the display control terminal via its internal Vio core. Changes in the panel indicator lights were observed to determine whether the software dynamic loading functioned normally. Each time the Vio core sent a trigger signal for dynamic loading, a stopwatch was immediately started. Timing was stopped upon observing a color change in the panel indicator lights, and the duration recorded for each stopwatch measurement.

After the indicator light color changes, the ILA core captures the regular pulse signal generated by the FPGA program's self-test module at the PDW output port to verify whether PDWs with correct pulse parameters are output. If the indicator light color changes normally and correct PDWs are output consistently, it indicates successful program switching and completion of the power IoT device information loading. Considering factors such as actual verification time and workload, this paper performed 30 consecutive dynamic loading tests to calculate the average completion time and success rate for dynamic loading of power IoT device information.

Table 1 presents the specific statistics for average loading time and success rate. Each power IoT device information loading completed in under 3.10 seconds, with the fastest taking only 1.52 seconds. The average loading completion time was 2.30 seconds. Considering manual timing errors and other factors, the actual information loading speed is exceptionally fast. Additionally, the panel indicator lights switched colors normally, and the success rate ranged between [99.19, 100.00]%, confirming the validity of the information loading.

*Table 1: Dynamic loading completion time and success rate*

| Number of trials | Loading completion time/s | Change of indicator light color | Loading success rate/% | Number of trials | Loading completion time/s | Change of indicator light color | Loading success rate/% |
|---|---|---|---|---|---|---|---|
| 1 | 2.18 | Normal | 100.00 | 16 | 2.38 | Normal | 100.00 |
| 2 | 1.52 | Normal | 99.98 | 17 | 2.68 | Normal | 100.00 |
| 3 | 2.28 | Normal | 99.87 | 18 | 2.81 | Normal | 99.99 |
| 4 | 2.21 | Normal | 100.00 | 19 | 2.69 | Normal | 99.87 |
| 5 | 2.08 | Normal | 99.19 | 20 | 2.22 | Normal | 100.00 |
| 6 | 2.28 | Normal | 99.58 | 21 | 2.78 | Normal | 100.00 |
| 7 | 2.79 | Normal | 100.00 | 22 | 2.08 | Normal | 100.00 |
| 8 | 2.42 | Normal | 100.00 | 23 | 2.25 | Normal | 100.00 |
| 9 | 2.29 | Normal | 100.00 | 24 | 2.99 | Normal | 99.90 |
| 10 | 1.98 | Normal | 100.00 | 25 | 2.51 | Normal | 99.89 |
| 11 | 2.58 | Normal | 100.00 | 26 | 2.02 | Normal | 100.00 |
| 12 | 2.13 | Normal | 99.99 | 27 | 3.04 | Normal | 100.00 |
| 13 | 2.07 | Normal | 99.87 | 28 | 2.23 | Normal | 100.00 |
| 14 | 2.31 | Normal | 100.00 | 29 | 3.07 | Normal | 100.00 |
| 15 | 2.78 | Normal | 99.79 | 30 | 2.97 | Normal | 100.00 |

# 4 Conclusion

This paper enhances the positioning accuracy of power IoT devices through geometric constraints while improving information loading efficiency with a delay filter. With a correction coefficient $\alpha$ set at 0.65, the error percentage ranges from 0.004% to 0.390%, indicating minimal positioning deviation. Data processed by the VFD filter concentrates in the time domain between 0.8s and 1.6s. All 30 information loading attempts completed within 3.10 seconds, achieving a maximum loading success rate of 100.00%. The geometry-constraint-based wireless positioning optimization method enables precise localization of IoT devices within the area, facilitating rapid device identification during data loading and reducing loading time. Additionally, the delayed loading approach prevents data from flooding in during a short time window, thereby improving the accuracy of loaded information.

# About the Authors

Hui Zhang (1976-02), male, Han Nationality, Jinhua, Zhejiang province, bachelor degree, engineer, research direction distribution network management.

Xiaofeng Lu (1980-08), male, Han Nationality, Jinhua, Zhejiang province, engineer, research direction distribution network design, construction and management.

Kai Kang (1987-03), male, Han Nationality, Jinhua, Zhejiang province, bachelor degree, assistant engineer, research direction power design management.

Huabo Mao (1979-10), male, Han Nationality, Jinhua, Zhejiang province, bachelor degree, assistant engineer, research direction power design management.

Honghong Zhu (1986-03), female, Han Nationality, Jinhua, Zhejiang province, Bachelor degree, engineer, research direction distribution network management.

Dawei Shao (1989-12), male, Han Nationality, Jinhua, Zhejiang province, bachelor degree, engineer, research direction distribution network management.

# References

[1] Tuballa, M. L., & Abundo, M. L. (2016). A review of the development of Smart Grid technologies. Renewable and Sustainable Energy Reviews, 59, 710-725.

[2] Paul, S., Rabbani, M. S., Kundu, R. K., & Zaman, S. M. R. (2014, January). A review of smart technology (Smart Grid) and its features. In 2014 1st International Conference on Non Conventional Energy (ICONCE 2014) (pp. 200-203). IEEE.

[3] Ghasempour, A. (2019). Internet of things in smart grid: Architecture, applications, services, key technologies, and challenges. Inventions, 4(1), 22.

[4] Saleem, Y., Crespi, N., Rehmani, M. H., & Copeland, R. (2019). Internet of things-aided smart grid: technologies, architectures, applications, prototypes, and future research directions. Ieee Access, 7, 62962-63003.

[5] Guerrero, J. I., García, A., Personal, E., Luque, J., & León, C. (2017). Heterogeneous data source integration for smart grid ecosystems based on metadata mining. Expert Systems with Applications, 79, 254-268.

[6] Figueiredo e Silva, P., Kaseva, V., & Lohan, E. S. (2018). Wireless positioning in IoT: A look at current and future trends. Sensors, 18(8), 2470.

[7] Pereira, F., Correia, R., Pinho, P., Lopes, S. I., & Carvalho, N. B. (2020). Challenges in resource-constrained IoT devices: Energy and communication as critical success factors for future IoT deployment. Sensors, 20(22), 6420.

[8] Gray, C., Ayre, R., Hinton, K., & Tucker, R. S. (2015, June). Power consumption of IoT access network technologies. In 2015 IEEE International Conference on Communication Workshop (ICCW) (pp. 2818-2823). IEEE.

[9] Fadel, E., Gungor, V. C., Nassef, L., Akkari, N., Malik, M. A., Almasri, S., & Akyildiz, I. F. (2015). A survey on wireless sensor networks for smart grid. Computer Communications, 71, 22-33.

[10] Liu, Y. (2012). Wireless sensor network applications in smart grid: recent trends and challenges. International Journal of Distributed Sensor Networks, 8(9), 492819.

[11] Voropai, N. (2020). Electric power system transformations: A review of main prospects and challenges. Energies, 13(21), 5639.

[12] Inci, M., Çelik, Ö., Lashab, A., Bayındır, K. Ç., Vasquez, J. C., & Guerrero, J. M. (2024). Power system integration of electric vehicles: A review on impacts and contributions to the smart grid. Applied Sciences, 14(6), 2246.

[13] Butt, O. M., Zulqarnain, M., & Butt, T. M. (2021). Recent advancement in smart grid technology: Future prospects in the electrical power network. Ain Shams Engineering Journal, 12(1), 687-695.

[14] Swain, A., Abdellatif, E., Mousa, A., & Pong, P. W. (2022). Sensor technologies for transmission and distribution systems: A review of the latest developments. Energies, 15(19), 7339.

[15] Morales-Velazquez, L., de Jesus Romero-Troncoso, R., Herrera-Ruiz, G., Morinigo-Sotelo, D., & Osornio-Rios, R. A. (2017). Smart sensor network for power quality monitoring in electrical installations. Measurement, 103, 133-142.

[16] Morello, R., Mukhopadhyay, S. C., Liu, Z., Slomovitz, D., & Samantaray, S. R. (2017). Advances on sensing technologies for smart cities and power grids: A review. IEEE Sensors Journal, 17(23), 7596-7610.

[17] Kim, D. Y., & Jung, M. (2017). Data transmission and network architecture in long range low power sensor networks for IoT. Wireless Personal Communications, 93(1), 119-129.

[18] Zhao, Y., Xia, S., Zhang, J., Hu, Y., & Wu, M. (2021). Effect of the digital transformation of power system on renewable energy utilization in China. Ieee Access, 9, 96201-96209.

[19] Shunxin, L., Yue, H., Yue, Y., Li, W., Pang, Y., & Zhao, Y. (2020, November). Power mechanism and strategy of digital transformation in power grid industry-Take State Grid Jibei Electric Power Company Limited as an example. In 2020 International Conference on Computer Science and Management Technology (ICCSMT) (pp. 340-345). IEEE Computer Society.

[20] Bayoumi, E. H. (2015). Power electronics in smart grid power transmission systems: a review. International Journal of Industrial Electronics and Drives, 2(2), 98-115.

[21] Al Mtawa, Y., Haque, A., & Halabi, T. (2022). A review and taxonomy on fault analysis in transmission power systems. Computation, 10(9), 144.